

General scheme of differential imaging employing weak measurement

Xiong Liu , An Wang, Junfan Zhu, Ling Ye, Rongchun Ge, Jinglei Du, Hong Zhang,* and Zhiyou Zhang [†]
College of Physics, Sichuan University, Chengdu 610064, China

 (Received 26 April 2022; accepted 10 August 2022; published 18 August 2022)

We propose and experimentally realize a general scheme of differential imaging employing the idea of weak measurement. We show that the weak coupling between the system of interest and a two-level ancilla can introduce a two-beam circuit after an arbitrary preselection of the ancilla. By choosing the postselection orthogonal to the preselection measurement, an effective imaging platform based on differential operations is achieved. Experimental results on both the Sagnac interferometer and ultrathin Wollaston prism demonstrate that our imaging scheme successfully yields the boundary information of complex geometric configurations.

DOI: [10.1103/PhysRevA.106.023518](https://doi.org/10.1103/PhysRevA.106.023518)

I. INTRODUCTION

As a strategy to go beyond strong projective measurement, weak measurement has attracted wide attention ever since its first proposal for yielding unreasonably large experimental results [1]. To get a large weak value, a postselected measurement which is almost orthogonal to the preselected state of the system is necessary. Aside from the pre- and postselections operations, a weak coupling between the system of interest and the meter is important, to make sure that the meter is not seriously suffering from dephasing (when tracing out the system) during the whole process. The exotic properties of weak measurement have made it an important research tool to tackle fundamental problems [2] and explore novel phenomena of quantum mechanics. Among the ongoing endeavors of applications of weak measurement are precision estimations [3–17], ultrasensitive sensors [18–22], and fundamental physics research [23–28]. However, to the best of our knowledge a plausible imaging scheme employing weak measurement has been missing up to now.

Boundaries are the places around which the properties of some physical distributions (like density, permittivity, etc.) change dramatically, and consequently are the homes of various exotic physical phenomena such as the optical spin Hall effect [7] and the dissipationless edge transport of the topological insulator [29,30] to name just a few. So it is important to recognize the boundaries of arbitrarily shaped configurations. Once the boundaries are identified, a decent image of the configuration is obtained. Optical analog differential operation is a physical method of achieving imaging. As a basic mathematical operation, differentiation is usually processed directly in digital operation. However, in some applications where real-time differential computation is required, such as in medical and satellite applications [31,32], analog operation offers a new opportunity to the electronic method. Traditionally, analog differential mathematical computations are

realized as analog computers [33,34], but these solutions are not used widely because of their large size and slow response. Optics provides us the opportunity of real-time mathematical operations, and intensive studies have been carried out to shrink the size and speed up the response [35–45]. Especially, Silva *et al.* suitably designed metamaterial blocks to perform a variety of mathematical operations, including differential operation [35]. Recently, others successfully applied the spin Hall effect of light to spatial differentiation [46–49], and proposed more optical differential operation models [50–52] with the insight of geometric phase, which will greatly enrich the technology of edge detection.

As a continuation of the endeavor of applications of weak measurement, in this paper we report a general and robust experimental scheme of imaging based on differential operation. To be more specific, we will try to image the boundaries of complex geometric distributions with weak measurement based optical analog differential operations. Our basic idea is shown in Fig. 1; the input wave of arbitrary function $\phi(r)$ passing through the imaging platform becomes the output wave, which is proportional to the standard differential function $\phi'(r)$, and is finally received by the detector. Preselection initializes the whole system by selecting the input of a two-level ancilla, such as polarization, and this serves as the operating handle of the differential calculator consisting of the weak measurement system, to which the input function can be loaded. The weak-coupling interaction ($\propto |p_1\rangle\langle p_1| - |p_2\rangle\langle p_2|$) introduces path-dependent evolution due to the energy splitting between these relevant paths, P_i . Finally, in order to achieve the differential operation a proper postselection is chosen to produce a phase difference of Π between the two paths. Because the pre- and postselections are perpendicular to each other, the intensity of the output wave is very small. Consequently, the input function is greatly compressed, which reduces the detector's load. It should be emphasized that the frequency bandwidth here is mainly decided by the response of the optical devices employed which can be replaced easily in our experimental scheme if necessary; as a result, our scheme could be employed for a much wider range of frequency bands compared to schemes based on resonant effect.

*hongzhang@scu.edu.cn

[†]zhangzhiyou@scu.edu.cn

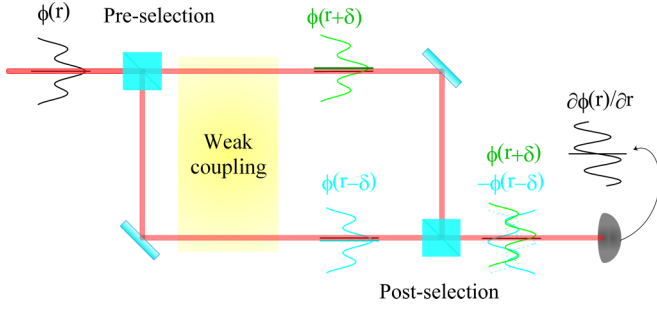


FIG. 1. Schematic diagram of weak measurement. Preselection, weak coupling, and postselection (perpendicular to the preselection) together make up the differential calculator; the output beam is collected at the detector (bottom right).

II. THEORETICAL ANALYSIS

Our physical platform consists of a two-level ancilla with observable \hat{A} , preselected as $|\Psi_{\text{pre}}\rangle = \alpha|0\rangle + \beta|1\rangle$, and the system of interest the information of which such as the geometric configuration is encoded in $\phi(r)$. The effective interaction Hamiltonian is given by $H = g\hat{A}k$, where g is the weak-coupling strength and k is the conjugate variable of the spatial coordinate r . Of special interest, we have $\hat{A} = |0\rangle\langle 0| - |1\rangle\langle 1|$ with $|0\rangle$ and $|1\rangle$ the orthogonal bases of the two-level ancilla. The physical distribution function $\phi(r)$ is Fourier transformed into $\tilde{\phi}(k)$ before the interaction is turned on. Due to the interaction between the system and the meter as represented by a unitary operation $\hat{U} = \exp(-igk\hat{A})$, the whole system is

$$\begin{aligned} |\Phi(k)\rangle &\equiv \langle k|\Phi\rangle = \hat{U}|\Psi_{\text{pre}}\rangle\tilde{\phi}(k) \\ &= (\alpha e^{-igk}|0\rangle + \beta e^{igk}|1\rangle)\tilde{\phi}(k). \end{aligned} \quad (1)$$

By inverse Fourier transform we obtain $|\Phi(r)\rangle = [\alpha\phi(r-g)|0\rangle + \beta\phi(r+g)|1\rangle]$, which means that after the interaction there is a split of size g between the $|0\rangle$ and $|1\rangle$ components. Then a special postselection perpendicular to the preselection state, i.e., $|\Psi_{\text{post}}^\perp\rangle = |\Psi_{\text{pre}}^\perp\rangle = \mu|0\rangle + \nu|1\rangle$, is chosen, where $|\mu|^2 + |\nu|^2 = 1$ and $\mu^*\alpha + \nu^*\beta = 0$. Finally, the whole system can be expressed as

$$\langle\Psi_{\text{pre}}^\perp|\Phi(r)\rangle = \mu^*\alpha[\phi(r-g) - \phi(r+g)]. \quad (2)$$

It is worth noting that the postselection gives a phase difference of π between the two paths $|0\rangle$ and $|1\rangle$. In weak measurement, the spatial distance over which the initial field of the image displays a considerable change (like an obvious deviation from a linear increase or decrease) is much larger than the typical distance decided by the coupling strength g , so the final output wave function is approximately proportional to the first-order differentiation of the input wave function:

$$\langle\Psi_{\text{pre}}^\perp|\Phi(r)\rangle \simeq -2\mu^*\alpha g\phi'(r). \quad (3)$$

However, if the postselection is introduced without the coordinate in Eq. (1) being transformed from k space to r space, the final output wave function is

$$\langle\Psi_{\text{pre}}^\perp|\Phi(k)\rangle \simeq -i2\mu^*\alpha gk\tilde{\phi}(k). \quad (4)$$

It is clear that the output beam is proportional to the function $k\tilde{\phi}(k)$, which is not the first-order differentiation of the input

function $\tilde{\phi}'(k)$ most of the time except for the Gaussian beam the first derivative of which is $k\tilde{\phi}(k)$. From Eqs. (3) and (4), it can be seen that the differential function appears only in the same space as the small split g . This observation indicates that the weak-coupling parameter and the input distribution should be in the same space to achieve the desired differential operation.

Although the theory shown is for a single photon, the same idea applies to a macroscopic beam, which is the case in our experiments in the next section. In the following, we will give a brief description of the parallel framework for electromagnetic waves at the classical limit.

Considering a plane wave, we define 0 and 1 as the two paths of evolution. Under the paraxial approximation, the incident and outgoing beams have the electric fields

$$E_i = \int [u_0^i\tilde{E}_0^i(k) + u_1^i\tilde{E}_1^i(k)]e^{ikr}dk, \quad (5)$$

$$E_o = \int [u_0^o\tilde{E}_0^o(k) + u_1^o\tilde{E}_1^o(k)]e^{ikr}dk, \quad (6)$$

where $u_{0(1)}^i$ and $u_{0(1)}^o$ correspond to the path-dependent incident and outgoing beams, respectively. To calculate the r -space spectral transfer function, we decompose the fields E_i and E_o into plane waves. The pre- and postselected states are described in matrix form as $V_{\text{pre}} = \begin{pmatrix} \alpha \\ \beta \end{pmatrix}$ and $V_{\text{post}} = \begin{pmatrix} \mu \\ \nu \end{pmatrix}$. Thus, the Fourier spectrum of the outgoing beam can be obtained as $\begin{pmatrix} \tilde{E}_0^o \\ \tilde{E}_1^o \end{pmatrix} = V_{\text{post}}^* U V_{\text{pre}} \begin{pmatrix} \tilde{E}_0^i \\ \tilde{E}_1^i \end{pmatrix}$ where U is the evolution operator incurred by the weak coupling, which can be evaluated through the geometric phase of the 0 and 1 paths under the paraxial approximation, as $U = \begin{pmatrix} \exp(-i\theta_g/2) & 0 \\ 0 & \exp(i\theta_g/2) \end{pmatrix}$. Here $\theta_g = 2gk$ is the geometric phase during weak coupling. Therefore, the evolution in k space can be effectively described by $H(k) \equiv \tilde{E}^o(k)/\tilde{E}^i(k) = V_{\text{post}}^* U V_{\text{pre}}$. Then, the spectral transfer function is obtained as

$$H(k) = \mu^*\alpha(e^{-igk} - e^{igk}). \quad (7)$$

For $g|k| \ll 1$, we have $H(k) \simeq -i2\mu^*\alpha gk$. As a result, the outgoing field in k space is $E^o(k) = -2\mu^*\alpha gkE^i(k)$. It should be noticed that the outgoing field is gk times the input field; in terms of light intensity, the output light is only $(gk)^2$ times the input light. In other words, the data of the input function are compressed to as few as $(gk)^2$ times. And in r space, the outgoing field reads

$$E^o(r) = -2\mu^*\alpha g \frac{\partial E^i(r)}{\partial r}, \quad (8)$$

which agrees with Eq. (3). In summary, the theory shows that the differential operation can be realized via an arbitrary two-level weak measurement system.

III. EXPERIMENTAL OBSERVATION

In this section, we show two experimental realizations of our weak measurement based imaging proposal: (1) a Sagnac interferometer based differential imaging platform, in which the Sagnac interferometer realizes the differential shear distance by a small deflection of the rotating mirror (RM), and at the output the spatial mathematical differential operation is

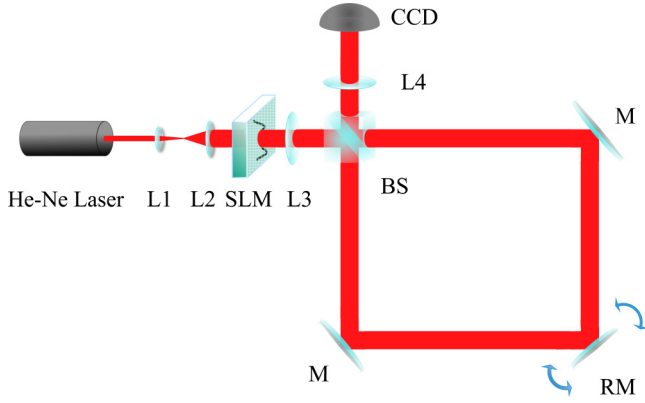


FIG. 2. Experimental setup: The light source is a He-Ne laser (wavelength $\lambda_0 = 632.8$ nm); L1 and L2, beam expanders; SLM, spatial light modulator; L3 and L4, lenses with focal lengths 250 mm; BS, beam splitter; M, mirror; RM, rotating mirror; CCD, Thorlabs BC106N-VIS.

achieved; and (2) a Wollaston prism based differential imaging platform, in which an ultrathin Wollaston prism performs the differential shear distance (δ), and the mathematical differential operation in the spatial domain is realized along with the whole weak measurement system.

A. Sagnac interferometer based differential imaging platform

In our Sagnac interferometer based differential imaging platform, the system consists of three cascaded sub-blocks: (i) a Fourier transform lens (L3); (ii) Sagnac interferometer, realizing three steps of weak measurement; and (iii) an inverse Fourier transform lens (L4) as shown in Fig. 2.

The laser from the He-Ne laser is expanded by a beam expander at the first step; it then obtains an image with specific spatial distribution as passing through the spatial light modulator (SLM), denoted as $|\psi_i\rangle = \int dr \phi_i(r)|r\rangle$, where r is the spatial coordinate. In the paraxial approximation, L3 accomplishes the Fourier transform of the image into the momentum space, i.e., $|\psi_i\rangle = \int dk \tilde{\phi}_i(k)|k\rangle$. When the light passes through the beam splitter (BS), it splits into two paths, propagating along the clockwise and counterclockwise directions, respectively. Here, the path freedom of the light beam constitutes a two-level system ($| \odot \rangle$ and $| \ominus \rangle$). In other words, the light is preselected as the state of the superposition of two paths, i.e., $|R_{\text{pre}}\rangle = \frac{1}{\sqrt{2}}(| \odot \rangle + i | \ominus \rangle)$, where i is the phase $\pi/2$ of the light induced as the counterclockwise path reflects at the BS. And the whole initial state is $|\Psi_i\rangle = |\psi_i\rangle |R_{\text{pre}}\rangle$. The rotating mirror (RM) is a mirror that can be rotated by a small angle, denoted as β , which tilts the lights in the clockwise and the counterclockwise paths slightly in opposite directions, $\Delta\theta = 4\beta$, and this tilt ($\Delta\theta$) leads to a small displacement of the transverse momentum of the beam ($\Delta k_x = k_0 \Delta\theta$). The observable of paths and the continuous transverse tilt together form the weak interaction, described by $\hat{U} = e^{-ik_x \hat{A} \delta/2}$ with $\delta = l \Delta\theta$, where $\hat{A} = | \odot \rangle \langle \odot | - | \ominus \rangle \langle \ominus |$ is the observable of paths; l is the distance from the RM to the charge-coupled device (CCD) [8], and k_x is the momentum in the x direction

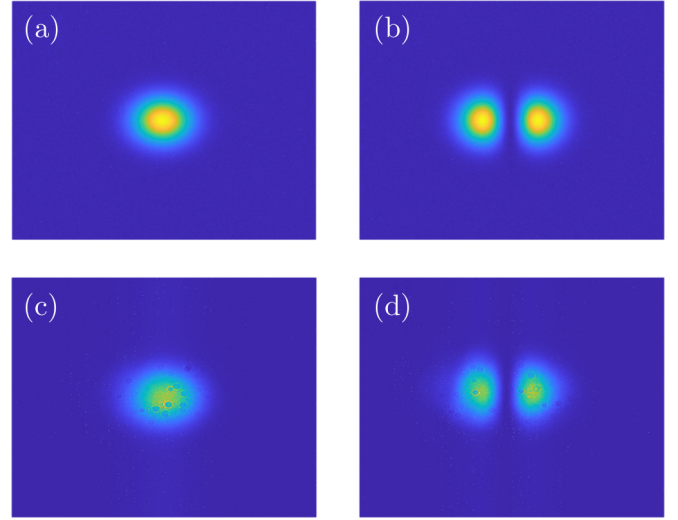


FIG. 3. Gaussian distributions and the differential images of them. (a, c) Simulated and experimental Gaussian distributions, respectively. (b, d) Corresponding differential images in the x direction.

for the RM rotating in the horizontal plane only. When the beams pass through the BS again, the postselection applies, $|R_{\text{post}}\rangle = \frac{1}{\sqrt{2}}(| \odot \rangle - i | \ominus \rangle)$, with the final state of light given by

$$|\Psi_f\rangle = \langle R_{\text{post}} | \hat{U} | \Psi_i \rangle = \frac{1}{2} \int dk \tilde{\phi}_i(k) (e^{-ik_x \delta/2} - e^{ik_x \delta/2}) |k\rangle. \quad (9)$$

After the inverse Fourier transform by L4, the outgoing state is

$$|\Psi_o\rangle = -\frac{1}{2} \int dr \frac{\partial \phi_i(x)}{\partial r} |r\rangle. \quad (10)$$

Finally, our CCD measures the light, which is the first derivative in the x direction of the specific spatial distribution image $\phi_i(r)$. To illustrate the spatial differentiation effect, we measure the outgoing field distribution under a Gaussian beam illumination firstly. Figures 3(c) and 3(d) show the measured intensity profiles for the incident and outgoing beams, respectively. To quantitatively illustrate the performance of spatial differentiation, the incident beam is numerically fitted with a Gaussian profile, and its differential function in the x direction is calculated numerically, as shown in Figs. 3(a) and 3(b), respectively. The experimental outgoing fields show a good agreement with the ideal spatial differentiation. Then, the spatial transfer function of the Sagnac interferometer based differential imaging platform is calculated based on experiments. From the relation of the incident and outgoing spatial spectra, we have the spatial transfer function, $H(k) = E^o(k)/E^i(k)$. The outgoing field distribution under a Gaussian beam can be measured with the device shown in Fig. 2,

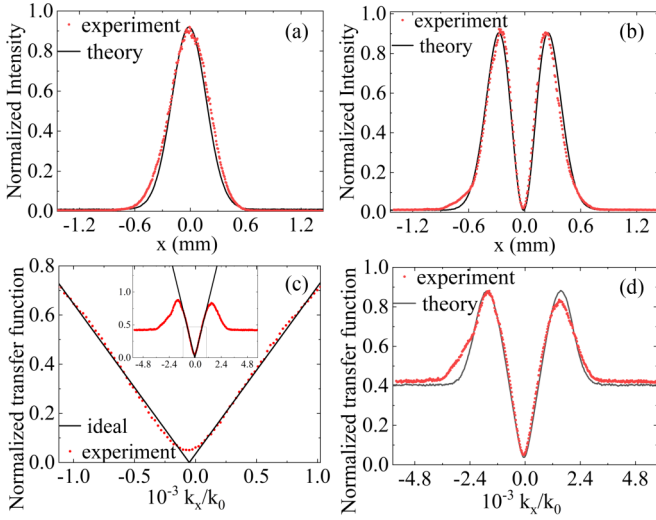


FIG. 4. Measurement of the spatial spectral transfer function. (a) Gaussian beam for $k_y = 0$. (b) The first derivative of the Gaussian beam in the x direction for $k_y = 0$. (c) Spatial spectral transfer function for $k_y = 0$. (d) Spatial spectral transfer function for $k_y = 0$ [consider a tiny random light noise (0.01%)]. Experimental results are shown in red dots, and theoretical results are in black lines.

i.e., the outgoing spatial spectrum is at the back focal plane of L4. Then we block arbitrarily one of the paths, and the incident spatial spectrum is at the back focal plane of L4. Since the CCD can only receive the intensity distribution of light in spatial space, we calculate the electric field with the equation of $|E(r)| = \sqrt{I(r)}$. With the help of L4, the spatial coordinate r is related to the momentum k , $r = fk/k_0$, where f is the focal distance of L4, so we obtain $E(k) = E(r)k_0/f$. Finally the spatial transfer function can be calculated as

$$H(k) = \sqrt{I_o(k)}/\sqrt{I_i(k)} = \sqrt{I_o(r)}/\sqrt{I_i(r)}, \quad (11)$$

and the theoretical transfer function is obtained by $H(k) = E'_G(k)/E_G(k)$, where $E_G(k)$ is the electric field of the Gaussian function. The results are shown in Fig. 4: it is clear from Fig. 4(c) that the experimental transfer function matches that of the theory well in the central region, but not in other regions, as a result of the pervasive noise. Even though it is tiny (<0.01%), the noise could seriously affect the experimental results since the amplitude of the Gaussian beam is small away from the central region. To roughly account for the ubiquitous noise residing in the laser beam, such as the randomly distributed speckles, we add a uniformly distributed random term, i.e., $H(k) = [E'_G(k) + c \times \text{rand}(k)]/[E_G(k) + c \times \text{rand}(k)]$, where c is less than 0.01% of the amplitude of the otherwise ideal Gaussian beam; then the theoretical and experimental results agree well with each other in all regions, as shown in Fig. 4(d). According to the differential imaging theory above, the differential operation can be performed in any direction, but here we only measure the derivative of the incident fields in the x direction as our RM in the Sagnac interferometer can only rotate in the horizontal plane (the x direction). Figure 5(a) shows the incident image of a disk generated with amplitude modulation by using the SLM, where the inside region of the circle is filled with light, while the

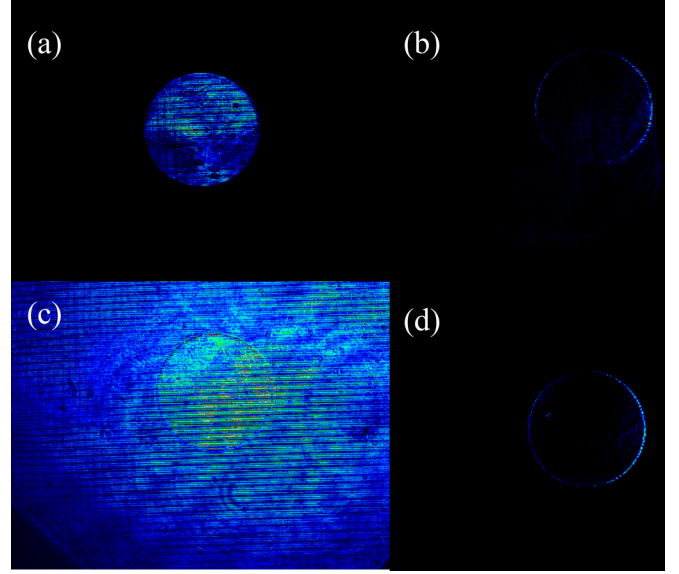


FIG. 5. Disk distributions and the differential images of them. (a, c) Incident images of disk distributions generated with amplitude and phase modulation, respectively. (b, d) Corresponding differential images in the x direction.

outside is dark. Figure 5(b) shows the measured outgoing intensity distribution. It clearly exhibits the outline of the disk with spatial differentiation. In Fig. 5(b), since the differentiation is along the x direction, the edges perpendicular to the x direction are most visible and those of the x direction are invisible. Furthermore, the edge of the input beam can be detected as long as it is not completely along the x direction.

Since the differentiation operates on the electric field rather than on the intensity, the platform can be used to detect the edge of the incident field either in the phase or in the amplitude distribution. To show such an effect, we also generate an incident field with phase modulation, as shown in Fig. 5(c); the disk is filled with light both inside and outside. Again, the outgoing light clearly exhibits the edge of the disk in the x direction as shown in Fig. 5(d). It should be noticed that the intensity of the right side of the circle is stronger than that of the left side, as shown in Figs. 5(b) and 5(d). The reason is that the light is not equally divided into two beams by the BS employed in the experiment. In order to show that general graphs can be differentially imaged by the platform, bell-shaped incident fields are generated. It can be seen from Fig. 6 that the platform can differentiate the incident field well whether it is amplitude or phase distribution. Especially for the phase distribution with a bright mess as shown in Fig. 6(c), the edge profile of the bell in the x direction is surprisingly clear after the operation of the differential platform, as shown in Fig. 6(d).

It can be seen from Figs. 5 and 6 that the output differential images carry only the edge information of the input images, and there is no light elsewhere; that is to say, the amount of data obtained by the CCD is greatly compressed, and as a consequence the detector's load is sharply decreased, which prevents the CCD from being oversaturated by too strong light.

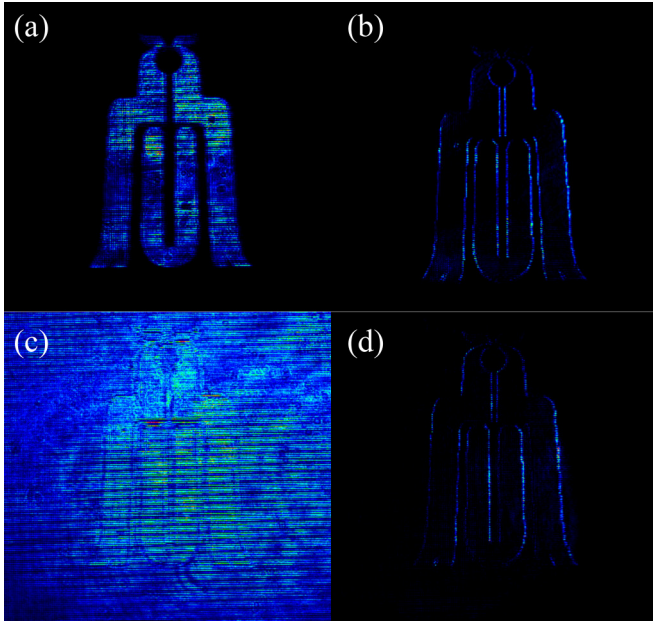


FIG. 6. Bell distributions and the differential images of them. (a, c) Bell distributions generated with amplitude and phase modulation, respectively. (b, d) Corresponding differential images in the x direction.

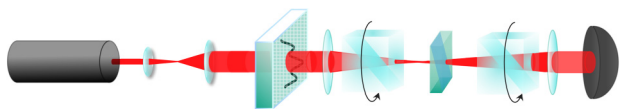
B. Wollaston prism based differential imaging platform

Our system of a Wollaston prism based differential imaging platform consists of five cascaded sub-blocks: (i) a Fourier transform lens (L3), (ii) a preselection (P1), (iii) a weak coupling (WP), (iv) a postselection (P2), and (v) an inverse Fourier transform lens (L4), as shown in Fig. 7.

As the laser passes through L3, the state of light is written as $|\psi_i\rangle = \int dk \hat{\phi}_i(k)|k\rangle$. P1 plays the role of preselection and preselects the light as

$$|\Psi_i\rangle = |\psi_{\text{pre}}\rangle|\psi_i\rangle, \quad (12)$$

where $|\psi_{\text{pre}}\rangle = \frac{1}{\sqrt{2}}(|o\rangle + |e\rangle)$ is the preselected polarization state of light, and $|o\rangle$ and $|e\rangle$ indicate ordinary and extraordinary light, respectively. WP plays the role of weak coupling; as a result of the effect of the ultrathin WP, ordinary and extraordinary light will split slightly from each other. Supposing the splitting distance is δ (about $20 \mu\text{m}$), then the weak interaction can be written as $|\Psi_{\text{int}}\rangle = \hat{U}|\Psi_i\rangle$, where $\hat{U} = \exp(-ik_d \hat{A} \delta/2)$ is the evolution operator; $\hat{A} = |o\rangle\langle o| - |e\rangle\langle e|$



He-Ne Laser L1 L2 SLM L3 P1 WP P2 L4 CCD

FIG. 7. Experimental setup: The light source is a He-Ne laser (wavelength $\lambda_0 = 632.8 \text{ nm}$). L1 and L2, beam expanders; SLM, spatial light modulator; P1 and P2, polarizers; L3 and L4, lenses with focal lengths 250 mm ; WP, an ultrathin Wollaston prism; CCD, Thorlabs BC106N-VIS.

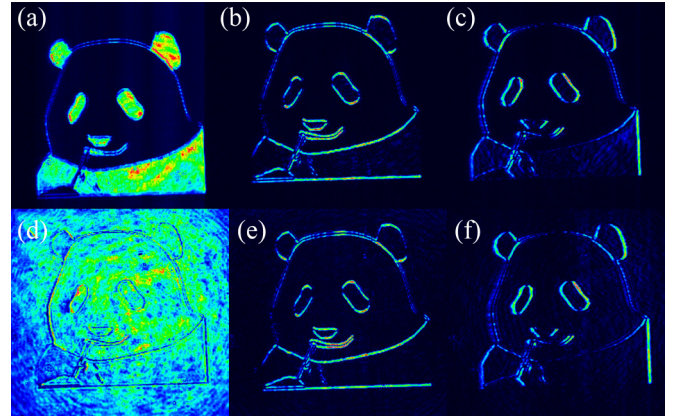


FIG. 8. Panda distributions and the differential images of them. (a, d) Panda distributions generated with amplitude and phase modulation, respectively. (b, e) Corresponding differential images in the y direction. (c, f) Corresponding differential images in the x direction.

is the observable operator and k_d is the momentum in the d direction (d direction means an arbitrary direction; in our experiments here, d is y or x). P2 is a postselected polarizer perpendicular to P1; the state of P2 is described as $|\psi_{\text{post}}\rangle = \frac{1}{\sqrt{2}}(|o\rangle - |e\rangle)$. And then the light is inverse Fourier transformed into the coordinate space by L4, so the state of outgoing light measured by the CCD is

$$|\Psi_o\rangle = -\frac{1}{2} \int dr \frac{\partial \phi_i(r)}{\partial r_d} |r\rangle. \quad (13)$$

From Eq. (13), the outgoing light is the first derivative in the d direction of the specific spatial distribution image $\phi_i(r)$.

Here we choose two directions to illustrate that weak measurement based differential schemes can operate on the field in any direction. The relevant results are shown in Fig. 8; both the edge information of phase and amplitude distributions of the incident fields (Panda) can be obtained. The incident amplitude spatial spectrum is measured by removing WP and rotating the polarizer P2 to the same direction as P1, as shown in Fig. 8(a). Figures 8(b) and 8(c) show the measured outgoing intensity distributions being differentiated in y and x directions, respectively. They clearly exhibit the outlines of Panda with spatial differentiation. The phase distributions are shown in Figs. 8(d)–8(f). More details are shown in the Appendix.

IV. CONCLUSION

In conclusion, we have proposed a general scheme of imaging employing the idea of weak measurement and listed two differential imaging platforms. Also, we have experimentally demonstrated the generality of spatial differentiation of the weak measurement differential system. Because the pre- and postselections are perpendicular to each other, the signal-to-noise ratio can be improved effectively while the background noise is reduced. Moreover, with no analog-to-digital conversion or other systematic delays, here mathematical operations have already got processed as the electromagnetic signals propagate through the weak measurement system. As a result, the data of the input image are greatly compressed before

being received by the CCD. Such designs prevent the detector from saturating itself with too strong light and thus missing the signal.

ACKNOWLEDGMENTS

This work is supported by the National Natural Science Foundation of China (Grant No. 11674234) and the Science Specialty Program of Sichuan University (Grant No. 2020SCUNL210). The authors thank Jiang Liu for the Panda picture.

APPENDIX: THE SPATIAL TRANSFER FUNCTION OF THE WOLLASTON PRISM BASED DIFFERENTIAL IMAGING PLATFORM AND ITS OPERATION ON CIRCLE DISTRIBUTIONS

The spatial transfer function of the Wollaston prism based differential imaging platform is calculated similarly to that of the Sagnac interferometer based differential imaging platform. First, we measure the field distribution under a Gaussian beam illumination at the back focal plane of L4. Figures 9(c) and 9(d) show the measured intensity profiles for the incident and outgoing beams, respectively. Then, the incident beam is numerically fitted with a Gaussian profile, as shown in Figs. 9(a) and 9(b). The experimental outgoing fields show a good agreement with the ideal spatial differentiation. Finally, the spatial transfer function is calculated as $H(k) = \sqrt{I_o(k)}/\sqrt{I_i(k)}$. As shown in Fig. 10, the results of experiment match the theory well in the central region, but not in other regions, and the reason is the same as the Sagnac interferometer based differential imaging platform.

The disk input function is also operated here to more clearly show the characteristics of the differential image in different directions. Figure 11(a) shows the incident image of a disk of light generated with amplitude modulation by using the SLM, where the inside of the disk is filled with light, while the outside is dark. Figures 11(b) and 11(c) show the measured

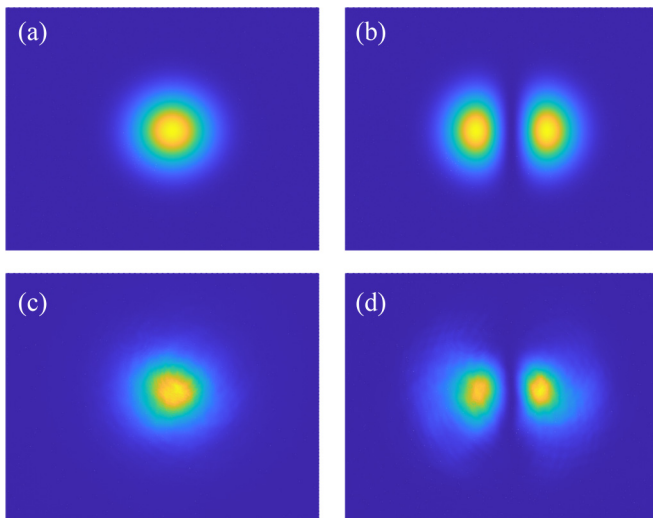


FIG. 9. Gaussian distributions and the differential images of them. (a, c) Simulated and experimental Gaussian distributions, respectively. (b, d) Corresponding differential images in the x direction.

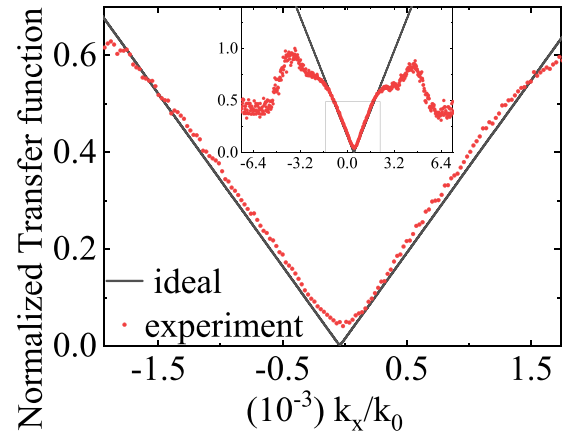


FIG. 10. Measurement of the spatial spectral transfer function for $k_y = 0$. Experimental results are shown in red dots, and theoretical results are in black lines.

outgoing intensities of y and x directions, respectively. They clearly exhibit the outline of the disk with spatial differentiation. In Fig. 11(b), since the differentiation is along the y direction, the edges perpendicular to the y direction are most visible and those of the y direction are invisible. Furthermore, as long as the edge is not completely along the y direction, it can be detected in the outgoing beam. The same thing happens in the x direction as shown in Fig. 11(c); the edges perpendicular to the x direction are most visible and those of the x direction are invisible.

As the differentiation operates on the electric field rather than on the intensity, the device can be used to detect an edge either in the phase or in the amplitude distribution of the incident field. To show such an effect, we also generate an incident field with phase modulation. Figure 11(d) shows the incident image of a circle of light generated with phase modulation; the circle is filled with light both inside and outside. Again, the outgoing light clearly exhibits the edge of the circle in the y direction or the x direction as shown in Figs. 11(e) and 11(f).

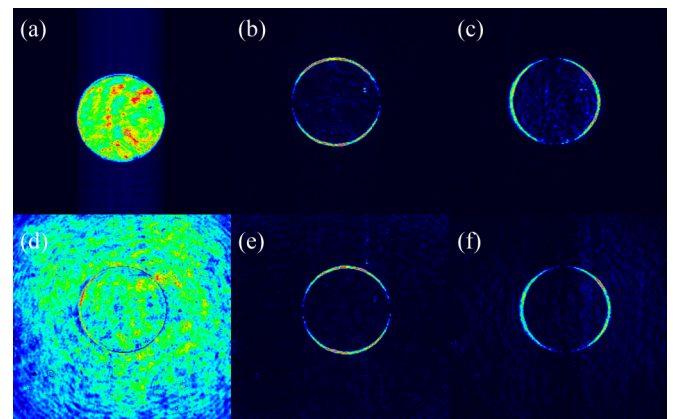


FIG. 11. Disk distributions and the differential images of them. (a, d) Disk distributions generated with amplitude and phase modulation, respectively. (b, e) Differential images of disks in the y direction. (c, f) Differential images of disks in the x direction.

- [1] Y. Aharonov, D. Z. Albert, and L. Vaidman, How the Result of a Measurement of a Component of the Spin of a Spin- $1/2$ Particle Can Turn Out to be 100, *Phys. Rev. Lett.* **60**, 1351 (1988).
- [2] S. Kocsis, B. Braverman, S. Ravets, M. J. Stevens, R. P. Mirin, L. K. Shalm, and A. M. Steinberg, Observing the average trajectories of single photons in a two-slit interferometer, *Science* **332**, 1170 (2011).
- [3] N. Brunner and C. Simon, Measuring Small Longitudinal Phase Shifts: Weak Measurements or Standard Interferometry? *Phys. Rev. Lett.* **105**, 010405 (2010).
- [4] D. J. Starling, P. B. Dixon, N. S. Williams, A. N. Jordan, and J. C. Howell, Continuous phase amplification with a Sagnac interferometer, *Phys. Rev. A* **82**, 011802(R) (2010).
- [5] X.-Y. Xu, Y. Kedem, K. Sun, L. Vaidman, C.-F. Li, and G.-C. Guo, Phase Estimation with Weak Measurement Using a White Light Source, *Phys. Rev. Lett.* **111**, 033604 (2013).
- [6] X. Qiu, L. Xie, X. Liu, L. Luo, Z. Li, Z. Zhang, and J. Du, Precision phase estimation based on weak-value amplification, *Appl. Phys. Lett.* **110**, 071105 (2017).
- [7] O. Hosten and P. Kwiat, Observation of the spin hall effect of light via weak measurements, *Science* **319**, 787 (2008).
- [8] P. B. Dixon, D. J. Starling, A. N. Jordan, and J. C. Howell, Ultrasensitive Beam Deflection Measurement via Interferometric Weak Value Amplification, *Phys. Rev. Lett.* **102**, 173601 (2009).
- [9] O. S. Magaña-Loaiza, M. Mirhosseini, B. Rodenburg, and R. W. Boyd, Amplification of Angular Rotations Using Weak Measurements, *Phys. Rev. Lett.* **112**, 200401 (2014).
- [10] Q. Wang, T. Li, L. Luo, Y. He, X. Liu, Z. Li, Z. Zhang, and J. Du, Measurement of hysteresis loop based on weak measurement, *Opt. Lett.* **45**, 1075 (2020).
- [11] B. Xia, J. Huang, C. Fang, H. Li, and G. Zeng, High-Precision Multiparameter Weak Measurement with Hermite-Gaussian Pointer, *Phys. Rev. Applied* **13**, 034023 (2020).
- [12] M. Liu, H. Li, G. Wang, B. Xia, J. Huang, and G. Zeng, High-precision temperature measurement with adjustable operating range based on weak measurement, *J. Phys. B* **54**, 085501 (2021).
- [13] C. Fang, J.-Z. Huang, H. Li, Y. Li, and G. Zeng, Improving precision of Mach-Zehnder interferometer with compensation employing weak measurement, *Appl. Phys. Lett.* **115**, 031101 (2019).
- [14] C. Fang, J.-Z. Huang, Y. Yu, Q. Li, and G. Zeng, Ultra-small time-delay estimation via a weak measurement technique with post-selection, *J. Phys. B* **49**, 175501 (2016).
- [15] G. Chen, P. Yin, W.-H. Zhang, G.-C. Li, C.-F. Li, and G.-C. Guo, Beating standard quantum limit with weak measurement, *Entropy* **23**, 354 (2021).
- [16] M. Yang, Q. Li, Z.-H. Liu, Z.-Y. Hao, C.-L. Ren, J.-S. Xu, C.-F. Li, and G.-C. Guo, Experimental observation of an anomalous weak value without post-selection, *Photon. Res.* **8**, 1468 (2020).
- [17] P. Yin, W.-H. Zhang, L. Xu, Z.-G. Liu, W.-F. Zhuang, L. Chen, M. Gong, Y. Ma, X.-X. Peng, G.-C. Li *et al.*, Improving the precision of optical metrology by detecting fewer photons with biased weak measurement, *Light Sci. Appl.* **10**, 1 (2021).
- [18] D. Li, Q. He, Y. He, M. Xin, Y. Zhang, and Z. Shen, Molecular imprinting sensor based on quantum weak measurement, *Biosens. Bioelectron.* **94**, 328 (2017).
- [19] L. Luo, X. Qiu, L. Xie, X. Liu, Z. Li, Z. Zhang, and J. Du, Precision improvement of surface plasmon resonance sensors based on weak-value amplification, *Opt. Express* **25**, 21107 (2017).
- [20] Y. Zhang, D. Li, Y. He, Z. Shen, and Q. He, Optical weak measurement system with common path implementation for label-free biomolecule sensing, *Opt. Lett.* **41**, 5409 (2016).
- [21] Y. Li, H. Li, J. Huang, C. Fang, M. Liu, C. Huang, and G. Zeng, High-precision temperature sensor based on weak measurement, *Opt. Express* **27**, 21455 (2019).
- [22] Y.-T. Wang, Z.-P. Li, S. Yu, Z.-J. Ke, W. Liu, Y. Meng, Y.-Z. Yang, J.-S. Tang, C.-F. Li, and G.-C. Guo, Experimental Investigation of State Distinguishability in Parity-Time Symmetric Quantum Dynamics, *Phys. Rev. Lett.* **124**, 230402 (2020).
- [23] K. Yokota, T. Yamamoto, M. Koashi, and N. Imoto, Direct observation of Hardy's paradox by joint weak measurement with an entangled photon pair, *New J. Phys.* **11**, 033011 (2009).
- [24] J. S. Lundeen and A. M. Steinberg, Experimental Joint Weak Measurement on a Photon Pair as a Probe of Hardy's Paradox, *Phys. Rev. Lett.* **102**, 020404 (2009).
- [25] N. Brunner, V. Scarani, M. Wegmüller, M. Legré, and N. Gisin, Direct Measurement of Superluminal Group Velocity and Signal Velocity in an Optical Fiber, *Phys. Rev. Lett.* **93**, 203902 (2004).
- [26] J. S. Lundeen, B. Sutherland, A. Patel, C. Stewart, and C. Bamber, Direct measurement of the quantum wavefunction, *Nature (London)* **474**, 188 (2011).
- [27] W.-W. Pan, X.-Y. Xu, Y. Kedem, Q.-Q. Wang, Z. Chen, M. Jan, K. Sun, J.-S. Xu, Y.-J. Han, C.-F. Li *et al.*, Direct Measurement of a Nonlocal Entangled Quantum State, *Phys. Rev. Lett.* **123**, 150402 (2019).
- [28] Z.-H. Liu, W.-W. Pan, X.-Y. Xu, M. Yang, J. Zhou, Z.-Y. Luo, K. Sun, J.-L. Chen, J.-S. Xu, C.-F. Li *et al.*, Experimental exchange of grins between quantum cheshire cats, *Nat. Commun.* **11**, 1 (2020).
- [29] X. Kou, S.-T. Guo, Y. Fan, L. Pan, M. Lang, Y. Jiang, Q. Shao, T. Nie, K. Murata, J. Tang *et al.*, Scale-Invariant Quantum Anomalous Hall Effect in Magnetic Topological Insulators beyond the Two-Dimensional Limit, *Phys. Rev. Lett.* **113**, 137201 (2014).
- [30] Y. Tokura, K. Yasuda, and A. Tsukazaki, Magnetic topological insulators, *Nat. Rev. Phys.* **1**, 126 (2019).
- [31] D. L. Pham, C. Xu, and J. L. Prince, Current methods in medical image segmentation, *Annu. Rev. Biomed. Eng.* **2**, 315 (2000).
- [32] R. J. Holyer and S. H. Peckinpugh, Edge detection applied to satellite imagery of the oceans, *IEEE Trans. Geosci. Remote Sensing* **27**, 46 (1989).
- [33] D. D. S. Price, A history of calculating machines, *Ieee Micro* **4**, 22 (1984).
- [34] A. B. Clymer, The mechanical analog computers of hannibal ford and william newell, *IEEE Annals of the History of Computing* **15**, 19 (1993).
- [35] A. Silva, F. Monticone, G. Castaldi, V. Galdi, A. Alù, and N. Engheta, Performing mathematical operations with metamaterials, *Science* **343**, 160 (2014).
- [36] Y. Hwang and T. J. Davis, Optical metasurfaces for subwavelength difference operations, *Appl. Phys. Lett.* **109**, 181101 (2016).

- [37] T. Zhu, Y. Zhou, Y. Lou, H. Ye, M. Qiu, Z. Ruan, and S. Fan, Plasmonic computing of spatial differentiation, *Nat. Commun.* **8**, 1 (2017).
- [38] Y. Fang, Y. Lou, and Z. Ruan, On-grating graphene surface plasmons enabling spatial differentiation in the terahertz region, *Opt. Lett.* **42**, 3840 (2017).
- [39] Z. Dong, J. Si, X. Yu, and X. Deng, Optical spatial differentiator based on subwavelength high-contrast gratings, *Appl. Phys. Lett.* **112**, 181102 (2018).
- [40] L. L. Doskolovich, D. A. Bykov, E. A. Bezus, and V. A. Soifer, Spatial differentiation of optical beams using phase-shifted Bragg grating, *Opt. Lett.* **39**, 1278 (2014).
- [41] A. Youssefi, F. Zangeneh-Nejad, S. Abdollahramezani, and A. Khavasi, Analog computing by brewster effect, *Opt. Lett.* **41**, 3467 (2016).
- [42] A. Pors, M. G. Nielsen, and S. I. Bozhevolnyi, Analog computing using reflective plasmonic metasurfaces, *Nano Lett.* **15**, 791 (2015).
- [43] N. V. Golovastikov, D. A. Bykov, L. L. Doskolovich, and E. A. Bezus, Spatial optical integrator based on phase-shifted bragg gratings, *Opt. Commun.* **338**, 457 (2015).
- [44] Z. Ruan, Spatial mode control of surface plasmon polariton excitation with gain medium: From spatial differentiator to integrator, *Opt. Lett.* **40**, 601 (2015).
- [45] C. Guo, M. Xiao, M. Minkov, Y. Shi, and S. Fan, Photonic crystal slab laplace operator for image differentiation, *Optica* **5**, 251 (2018).
- [46] T. Zhu, Y. Lou, Y. Zhou, J. Zhang, J. Huang, Y. Li, H. Luo, S. Wen, S. Zhu, Q. Gong *et al.*, Generalized Spatial Differentiation from the Spin Hall Effect of Light and its Application in Image Processing of Edge Detection, *Phys. Rev. Applied* **11**, 034043 (2019).
- [47] T. Zhu, J. Huang, and Z. Ruan, Optical phase mining by adjustable spatial differentiator, *Adv. Photonics* **2**, 016001 (2020).
- [48] D. Xu, S. He, J. Zhou, S. Chen, S. Wen, and H. Luo, Optical analog computing of two-dimensional spatial differentiation based on the brewster effect, *Opt. Lett.* **45**, 6867 (2020).
- [49] S. He, J. Zhou, S. Chen, W. Shu, H. Luo, and S. Wen, Spatial differential operation and edge detection based on the geometric spin hall effect of light, *Opt. Lett.* **45**, 877 (2020).
- [50] J. Zhou, H. Qian, J. Zhao, M. Tang, Q. Wu, M. Lei, H. Luo, S. Wen, S. Chen, and Z. Liu, Two-dimensional optical spatial differentiation and high-contrast imaging, *Natl. Sci. Rev.* **8**, nwaa176 (2021).
- [51] J. Zhou, H. Qian, C.-F. Chen, J. Zhao, G. Li, Q. Wu, H. Luo, S. Wen, and Z. Liu, Optical edge detection based on high-efficiency dielectric metasurface, *Proc. Natl. Acad. Sci. USA* **116**, 11137 (2019).
- [52] W. Xu, X. Ling, D. Xu, S. Chen, S. Wen, and H. Luo, Enhanced optical spatial differential operations via strong spin-orbit interactions in an anisotropic epsilon-near-zero slab, *Phys. Rev. A* **104**, 053513 (2021).